Nonlinear magnetohydrodynamics by Galerkin-method computation

Xiaowen Shan, David Montgomery, and Hudong Chen
Department of Physics and Astronomy, Dartmouth College, Hanover, New Hampshire 03755-3528
(Received 26 November 1990; revised manuscript received 24 July 1991)

A fully spectral numerical code is used to explore the properties of voltage-driven dissipative magnetofluids inside a periodic cylinder with circular cross section. The trial functions are orthonormal eigenfunctions of the curl (Chandrasekhar-Kendall functions). Transitions are observed from axisymmetric resistive equilibria without flow to helically deformed laminar states with flow, and between pairs of helical laminar states with different pairs of poloidal and toroidal m and n numbers. States of minimum energy-dissipation rate seem to be preferred. At high values of the pinch ratio, fully developed magnetohydrodynamic turbulence is observed.

PACS number(s): 52.30.−q, 52.55.Ez, 52.55.Fa, 47.65.+a

I. INTRODUCTION

This article reports some results from a computational method of exploring electrically driven, dissipative states of a conducting fluid. The situation contains much of the essential magnetohydrodynamics (MHD) of confined fusion plasmas in a torus. However, due to the lack of good internal pointwise diagnostics for the MHD fields in the present generation of tokamaks and toroidal Z pinches, numerical computations provide the possibility of much more detailed descriptions of the dynamical behavior than presently imaginable laboratory measurements do. The price is, of course, the necessary omission of some of the non-MHD features of a real plasma.

The computations reported here originate in an earlier set performed a few years ago [1] with a pseudospectral code interior to a rigid, perfectly conducting cylinder with square cross section and periodically identified ends. Those investigations started from a position of considerably less understanding than we now have of just what to expect. The Dahlburg *et al.* computations [1] had to be prepared for essentially anything to happen. The history of MHD computation had often been one of freezing out dynamically important phenomena by assuming symmetries at the outset that were not satisfied by the phenomena that turned out eventually most important.

The square-cylinder computations led, among other things, to one result that was robust and unexpected: a transition, above certain critical thresholds in the applied toroidal voltage, to a nonaxisymmetric state involving helical distortions of the current channel and a small but nontrivial amount of flow in the form of paired helical vortices. In the presence of spatially and temporally variable temperatures and temperature-dependent transport coefficients, the helical states could persist even while executing superimposed "sawtooth" oscillations [2].

A theoretical explanation of the behavior was sought and the best explanation so far has seemed to be one of attributing the presence of the helical MHD states to their lower rate of energy dissipation due to resistivity and viscosity [3]. An analytical solution was constructed [4] through the first three terms in a perturbation series (with the expansion parameter being formally the ratio of the helical magnetic components to the larger axisymmetric one), which showed that the steady-state solution to the MHD equations bifurcated at the appearance of the first linear (nonideal) instability. The unstable eigenmode [5] was constructed of Chandrasekhar-Kendall [6] helical eigenfunctions of the curl and formed the variable helical part of the nonaxisymmetric solution. This helical equilibrium was shown to have a lower energy dissipation rate than the axisymmetric one. Visual comparisons of surfaces of constant values of the field components and amplitudes, between analytically calculated and numerically computed cases, were encouraging enough to suggest further exploitation of the Chandrasekhar-Kendall functions [7].

A three-mode (Lorenz-like [8]) truncated Galerkin-method computation was explored by Chen, Shan, and Montgomery [9]. Near the threshold at which the phase-space point corresponding to the axisymmetric state ("axisymmetric fixed point") became linearly unstable, the three-mode model exhibited behavior that was qualitatively the same as the well-resolved computations [1,2] and the minimum-dissipation theory [4,7] had suggested: relaxation to the steady state of lower energy-dissipation rate, represented by a helical fixed point of the three-mode dynamical system. It was also suggested [9] that, because of the ease with which the Chandrasekhar-Kendall functions seemed to incorporate economically the results that had originated in the earlier well-resolved ($\sim 3\times 10^4$ degrees of freedom) MHD computations [1], they might be a useful expansion basis for a many-mode spectral computation.

In Sec. II we describe the construction of such a spectral code. A recent completeness theorem due to Yoshida and Giga [10] fills in what had been a worrisome gap in the mathematical underpinnings of such an expansion. Though the ultimate operation of the code is rather simple, the analysis involved in its construction is not altogether standard. One motivation in Sec. II is to put some of the details on record before proceeding with a set of applications that may extend well into the future. Some of these applications are presented in Sec. III and will

now be described briefly.

Formation of helical states is discussed first, in some detail, in Sec. III. It seems appropriate to characterize the various axisymmetric and helical regimes by three dimensionless parameters. They are (i) the Lundquist number $S \equiv C_A L/\eta$, where C_A is a toroidal Alfvén speed, L is a characteristic length scale such as the cylinder radius, and η is the magnetic diffusivity; (ii) the Hartmann number H, which will be defined here as $H \equiv C_A L/\sqrt{\eta\nu}$, with ν the kinematic viscosity; and (iii) the pinch ratio for the *axisymmetric, zero-flow state* $\Theta_0 = \overline{B}_\varphi / \langle B_z \rangle$, where $\overline{B}_\varphi$ is the wall-averaged poloidal magnetic field and $\langle B_z \rangle$ is the volume-averaged toroidal magnetic field. Θ_0 is to be carefully distinguished from the true pinch ratio Θ which, once the helical deformations set in, can be markedly lower than Θ_0. The onset of the helical states occurs as one crosses, moving up and to the left, a generally rising curve [7] in a plane whose x,y axes are H^{-2} and Θ_0. The essential laminar dissipative capability of the fluid is measured by H^{-2}, and Θ_0 measures how hard it is being driven. Θ_0 is proportional to the toroidal electric field at the wall.

The range of values of Θ_0 thoroughly explored here is typically $\lesssim 2.5$. In the laboratory setting, Θ_0 for a tokamak ($2\pi a/(L_z q)$, where a is the radius of the periodic cylinder, L_z is its length, and q is the "safety factor" [11]) is always less than 1, and for a toroidal Z pinch [12] it is greater than 1. Our measured Θ values, in the helical states, go up to about 2. In this region we see no final-state behavior that could reasonably be called "turbulent" for the S and H values we explore. (In fact, the laminar helical states appear to become time independent.) These S and H values are very low (of the order of 100) relative to laboratory values, which are often in excess of 10^5 or 10^6. The situation is much like that in fluid mechanics where computational Reynolds numbers are, and are likely to remain, much smaller than laboratory or geophysical Reynolds numbers. In the future, we plan to explore higher values of S and H, but they seem likely to stay below 10^4 in the near-term future, an unfortunate fact of life for the numericist. It has become apparent that as long as Θ_0 barely exceeds the critical pinch ratio for a given H^{-2}, the helical states will appear regardless of the value of H^{-2}. This implies that the qualitative behavior just above the threshold is independent of H^{-2}, within the MHD approximation.

In addition to the detailed exploration of the low-pinch-ratio investigations, we have also explored the case $\Theta_0 \cong 12.34$ (corresponding to a computed pinch ratio $\Theta \cong 4.8$) in enough detail to show that it is fully turbulent. Between $\Theta_0 \cong 2.5$ and 12.34, therefore, there is a transition to MHD turbulence, and we plan to explore this transition in detail in a future investigation; here we are content to assert its existence. It is to be expected that it will occur for lower Θ_0 as higher S and H values are reached.

The routes by which the $\Theta_0 \lesssim 2$ helical states can be reached can be varied by varying the scenario by which the applied toroidal voltage is taken up to its maximum. Several of these are described in Sec. III. Then some of the details of the turbulent ($\Theta_0 \cong 12.34$, $\Theta \cong 4.8$) state are presented. Finally, in Sec. IV the results are discussed and future possibilities are analyzed.

II. ANALYTICAL BASIS FOR THE COMPUTATION

The equations solved are those of uniform-density, incompressible, viscous resistive MHD. They are, in a familiar set of dimensionless ("Alfvénic") variables,

$$\frac{\partial \mathbf{v}}{\partial t} = \mathbf{v}\times\boldsymbol{\omega} + \mathbf{j}\times\mathbf{B} - \nabla p + \nu\nabla^2\mathbf{v} , \tag{1}$$

$$\frac{\partial \mathbf{B}}{\partial t} = \nabla\times(\mathbf{v}\times\mathbf{B}) - \eta\nabla\times\mathbf{j} = -\nabla\times\mathbf{E} , \tag{2}$$

with the electric field $\mathbf{E}$ given by

$$\mathbf{E} = -\mathbf{v}\times\mathbf{B} + \eta\mathbf{j} = -\frac{\partial \mathbf{A}}{\partial t} + \nabla\Phi . \tag{3}$$

Here, $\mathbf{v}$ is the velocity field, $\mathbf{B}$ is the magnetic field, and $\mathbf{j} = \nabla\times\mathbf{B}$ is the current density. The kinematic viscosity and magnetic diffusivity are ν and η, respectively, and may be thought of as the reciprocals of Reynolds-like numbers, both much less than 1. (Both ν and η will be taken here as spatially uniform and constant, and typically equal to 0.045; there is no denying that smaller values with allowed variability would be desirable for real-life laboratory comparisons.) Both $\mathbf{v}$ and $\mathbf{B}$ are solenoidal. $\mathbf{A}$ is the vector potential for which $\mathbf{B} = \nabla\times\mathbf{A}$ and $\nabla\cdot\mathbf{A} = 0$, while Φ is a scalar potential determined by solving $\nabla^2\Phi = -\nabla\cdot(\mathbf{v}\times\mathbf{B})$. The pressure p is determined by taking the divergence of Eq. (1), using $\nabla\cdot\partial\mathbf{v}/\partial t = 0$, and solving the resulting Poisson equation for $p = p(\mathbf{v},\mathbf{B})$. This p is the mechanical pressure plus $v^2/2$. The system of equations (1)–(3) is regarded as being electrically driven by demanding that the axial electric field shall have a nonvanishing spatial average over the boundary.

The boundary conditions to be imposed on $\mathbf{v}$ and $\mathbf{B}$ are $\mathbf{v}\cdot\hat{\mathbf{n}} = 0$ and $\mathbf{B}\cdot\hat{\mathbf{n}} = 0$, where $\hat{\mathbf{n}} = \hat{\mathbf{e}}_r$ is the unit normal to a right circular cylinder at radius $r = a$ (cylindrical coordinates). Periodic boundary conditions are assumed in the z coordinate with spatial period L_z. The perfect conductor at $r = a$ is assumed to be coated with a thin layer of insulating dielectric, so that $\mathbf{j}\cdot\hat{\mathbf{n}} = 0$ at $r = a$, also. For the vorticity $\boldsymbol{\omega} = \nabla\times\mathbf{v}$, we assume that $\boldsymbol{\omega}\cdot\hat{\mathbf{n}} = 0$ at $r = a$, which is implied by, but does not imply, no-slip viscous boundary conditions; the inability to impose fully no-slip boundary conditions on $\mathbf{v}$ is regarded as a shortcoming in the formulation of the problem that it would ultimately be desirable to lift. It is to be expected that fully no-slip boundary conditions would impose a $\mathbf{v}$-field boundary layer near the wall which the present computation does not apprehend. The magnetic field $\mathbf{B}$ is divided into a uniform dc axial part $\mathbf{B}_0$ plus a spatially and temporally variable part $\mathbf{b}$.

Both $\mathbf{b}$ and $\mathbf{v}$ will be expanded in terms of Chandrasekhar-Kendall orthonormal eigenfunctions of the curl [5,6]. These are defined in terms of solutions to the scalar wave equation $(\nabla^2 + \lambda^2)\psi = 0$, where the eigen-

value λ is yet to be determined. For ψ we will have

$$\psi_{nmq}=J_m(\gamma_{nmq}r)e^{(im\varphi-ik_nz)}\ , \tag{4}$$

where $k_n=2\pi n/L_z$, $n=0,\pm1,\pm2,\ldots$, $m=0,\pm1,\pm2,\ldots$, and $q=1,2,3,\ldots$ (three integers are required to index the functions). $\lambda^2_{nmq}=k_n^2+\gamma^2_{nmq}$. We define the expansion functions by

$$\mathbf{A}_{nmq}=I^{-1/2}_{nmq}[\lambda_{nmq}\nabla\psi_{nmq}\times\hat{\mathbf{e}}_z+\nabla\times(\nabla\psi_{nmq}\times\hat{\mathbf{e}}_z)]\ , \tag{5}$$

where I_{nmq} is defined as the normalization constant required to make

$$(\mathbf{A}_{nmq},\mathbf{A}_{nmq})=\frac{1}{V}\int_V\mathbf{A}_{nmq}\cdot\mathbf{A}^*_{nmq}d^3x=1\ , \tag{6}$$

where the integral runs over the interior of the cylinder $0\le r<a$, $0\le z\le L_z$, and $V=\pi a^2L_z$.

The $\mathbf{A}_{nmq}$ can be made orthonormal for a proper choice of γ_{nmq} for $n^2+m^2>0$. Determining the γ_{nmq} and λ_{nmq} by $\mathbf{A}_{nmq}\cdot\hat{\mathbf{n}}=0$ at $r=a$ is the proper choice. Clearly all the $\mathbf{A}_{nmq}$ with $n^2+m^2>0$ are orthogonal to the $\mathbf{A}_{00q}$. γ_{nmq} is always greater than 0, but both signs of λ_{nmq} must be allowed.

The $\mathbf{A}_{00q}$ require a little care, since the γ_{00q} are not determined by the boundary condition $\mathbf{A}_{00q}\cdot\hat{\mathbf{n}}=0$. A natural choice to determine γ_{00q} is to require $\mathbf{A}_{00q}$ to be "fluxless": i.e., $\int\mathbf{e}_z\cdot\mathbf{A}_{00q}d^2x=0$, where the integral runs over the cross section of the cylinder. Since $\mathbf{j}=\nabla\times\mathbf{B}$ and we wish to permit the possibility of a net current in the z direction, the expansion functions of $\mathbf{B}$ and $\mathbf{j}$ must then be supplemented by $\hat{\mathbf{e}}_z$ and $r\hat{\mathbf{e}}_\varphi/2$, which correspond to the net flux of the magnetic field and the current density, respectively.

The set of functions $\{\mathbf{A}_{nmq}\}$, truncated at some level, together with $r\hat{\mathbf{e}}_\varphi/2$ and $\hat{\mathbf{e}}_z$, span a subspace $\mathbb{S}$ of the Hilbert space $\mathbb{H}$ in which the exact solution of Eqs. (1)–(3) lies. Note that Eqs. (1)–(3) may be written symbolically as

$$\frac{dy}{dt}=F(y)\ , \tag{7}$$

where y is the exact solution. We may define $\mathcal{P}$ as the projection operator $\mathcal{P}$: $\mathbb{H}\to\mathbb{S}$. Under a Galerkin approximation [13], our approximate solution $\tilde{y}$ will satisfy

$$\frac{d\tilde{y}}{dt}=\mathcal{P}(F(\tilde{y}))\ , \tag{8}$$

where $\tilde{y}$ is the approximate solution which lies in $\mathbb{S}$. It can be easily shown that such an approximate solution will conserve all the quadratic ideally conserved quantities of the original differential equations (1)–(3) such as total energy, magnetic helicity, and cross helicity. We have verified these conservation laws numerically, typically to an accuracy of one part in 10^6 over 10 poloidal Alfvén transit times.

Since $r\hat{\mathbf{e}}_\varphi/2$ is not orthogonal to $\{\mathbf{A}_{00q}\}$, we define a new basis vector $\mathbf{A}_0$, by using the Gram-Schmidt orthogonalization procedure, as

$$\mathbf{A}_0=\frac{r}{2}\hat{\mathbf{e}}_\varphi-\sum_q\alpha_q\mathbf{A}_{00q}\ , \tag{9}$$

$$\alpha_q=\frac{1}{V}\int_V\frac{r}{2}\hat{\mathbf{e}}_\varphi\cdot\mathbf{A}_{00q}d^3x\ , \tag{10}$$

so that the projection operator $\mathcal{P}$ takes a simpler form. (An alternative method which is equivalent in effect is to use the dual basis of the expansion functions as the test functions.)

We write, in general,

$$\mathbf{B}=j_0\mathbf{A}_0+B_0\hat{\mathbf{e}}_z+\sum_{n,m,q}\xi^B_{nmq}\mathbf{A}_{nmq}$$
$$=\frac{j_0r}{2}\hat{\mathbf{e}}_\varphi+B_0\hat{\mathbf{e}}_z+\sum_{n,m,q}\tilde{\xi}^B_{nmq}\mathbf{A}_{nmq}\ , \tag{11}$$

$$\mathbf{j}=j_0\nabla\times\mathbf{A}_0+\sum_{n,m,q}\lambda_{nmq}\xi^B_{nmq}\mathbf{A}_{nmq}$$
$$=j_0\hat{\mathbf{e}}_z+\sum_{n,m,q}\lambda_{nmq}\tilde{\xi}^B_{nmq}\mathbf{A}_{nmq}\ , \tag{12}$$

$$\mathbf{v}=\omega_0\mathbf{A}_0+\sum_{n,m,q}\xi^V_{nmq}\mathbf{A}_{nmq}$$
$$=\frac{\omega_0r}{2}\hat{\mathbf{e}}_\varphi+\sum_{n,m,q}\tilde{\xi}^V_{nmq}\mathbf{A}_{nmq}\ , \tag{13}$$

$$\omega=\omega_0\nabla\times\mathbf{A}_0+\sum_{n,m,q}\lambda_{nmq}\xi^V_{nmq}\mathbf{A}_{nmq}$$
$$=\omega_0\hat{\mathbf{e}}_z+\sum_{n,m,q}\lambda_{nmq}\tilde{\xi}^V_{nmq}\mathbf{A}_{nmq}\ . \tag{14}$$

Here, ξ^B_{nmq} and ξ^V_{nmq} are complex, time-dependent expansion coefficients which are the dynamical coordinates of the problem, j_0 and ω_0 are functions of time only, while B_0 is a constant (the imposed dc magnetic field). $\tilde{\xi}^B_{nmq}$ and $\tilde{\xi}^V_{nmq}$ are introduced for convenience in calculating the right-hand side of the MHD equations (1)–(3) and are defined by

$$\tilde{\xi}^B_{nmq}=\begin{cases}\xi^B_{nmq}, & m^2+n^2\neq0\\ \xi^B_{nmq}-j_0\alpha_q, & m=n=0\ ,\end{cases} \tag{15}$$

$$\tilde{\xi}^V_{nmq}=\begin{cases}\xi^V_{nmq}, & m^2+n^2\neq0\\ \xi^V_{nmq}-\omega_0\alpha_q, & m=n=0\ .\end{cases} \tag{16}$$

The computations are done with the expansions into the orthogonal sets, as represented in the first lines of Eqs. (11)–(14). In the second lines of Eqs. (11)–(14), the series has been *formally* rearranged to combine the components of $\mathbf{A}_0(\mathbf{r})$ into the sums over the Chandrasekhar-Kendall functions, and to show that giving the full set of ξ_{nmq} is *algebraically* equivalent to giving the $\tilde{\xi}_{nmq}$.

$\{\mathbf{A}_0,\hat{\mathbf{e}}_z,\mathbf{A}_{nmq}\}$ forms a set of orthogonal basis functions in which Galerkin's method amounts to substituting the expansions (11)–(14) into Eqs. (1)–(3) on both sides, taking inner products with the $\mathbf{A}_{nmq}$, and picking off what are in effect ordinary first-order differential equations for the expansion coefficients. At the first stage,

$$\frac{\partial}{\partial t}\xi^V_{nmq}=\frac{1}{V}\int_V \mathbf{A}^*_{nmq}\cdot[\mathbf{v}\times\boldsymbol{\omega}+\mathbf{j}\times\mathbf{B}-\nabla p+\nu\nabla^2\mathbf{v}]d^3x\ , \tag{17}$$

$$\frac{\partial}{\partial t}\xi^B_{nmq}=\frac{1}{V}\int_V \mathbf{A}^*_{nmq}\cdot[\nabla\times(\mathbf{v}\times\mathbf{B})-\eta\nabla\times\mathbf{j}]d^3x\ , \tag{18}$$

$$\|\mathbf{A}_0\|^2\frac{\partial}{\partial t}\omega_0=\frac{1}{V}\int_V \mathbf{A}_0\cdot[\mathbf{v}\times\boldsymbol{\omega}+\mathbf{j}\times\mathbf{B}-\nabla p+\nu\nabla^2\mathbf{v}]d^3x\ , \tag{19}$$

$$\|\mathbf{A}_0\|^2\frac{\partial}{\partial t}j_0=\frac{1}{V}\int_V \mathbf{A}_0\cdot[\nabla\times(\mathbf{v}\times\mathbf{B})-\eta\nabla\times\mathbf{j}]d^3x\ , \tag{20}$$

where

$$\|\mathbf{A}_0\|^2=\frac{1}{V}\int_V \mathbf{A}_0\cdot\mathbf{A}_0 d^3x=a^2\left[\frac{1}{8}-\sum_{\gamma_q}\frac{1}{(\gamma_{00q}a)^2}\right]. \tag{21}$$

Because all the spatial dependences of the fields have been transformed away, the partial derivatives with respect to time, in Eqs. (17)–(20) and hereafter, are in effect total derivatives.

Performing the integrals in Eqs. (17)–(20) is very tedious and the result is

$$\frac{\partial}{\partial t}\xi^V_{nmq}=\sum_{n',m',q'}\sum_{n'',m'',q''}\lambda_{n''m''q''}(\xi^V_{n'm'q'}\xi^V_{n''m''q''}-\xi^B_{n'm'q'}\xi^B_{n''m''q''})C_{nmq}\begin{bmatrix}n' & m' & q'\\ n'' & m'' & q''\end{bmatrix}$$
$$+i\left[\frac{m}{2}+\frac{k_n}{\lambda_{nmq}}\right](j_0\xi^B_{nmq}-\omega_0\xi^V_{nmq})-ik_nB_0\xi^B_{nmq}-\nu\lambda^2_{nmq}\xi^V_{nmq}\ , \tag{22}$$

$$\frac{\partial}{\partial t}\xi^B_{nmq}=\sum_{n',m',q'}\sum_{n'',m'',q''}\lambda_{nmq}\xi^V_{n'm'q'}\xi^B_{n''m''q''}C_{nmq}\begin{bmatrix}n' & m' & q'\\ n'' & m'' & q''\end{bmatrix}+\frac{im}{2}(j_0\xi^V_{nmq}-\omega_0\xi^B_{nmq})-ik_nB_0\xi^V_{nmq}-\eta\lambda^2_{nmq}\xi^B_{nmq}\ , \tag{23}$$

$$\|\mathbf{A}_0\|^2\frac{\partial}{\partial t}\omega_0=F_0-\nu_0\omega_0+\nu\sum_q\alpha_q\lambda^2_{00q}\xi^V_{00q}+\sum_{n,m,q',q''}\mathcal{D}_{nmq'q''}(\xi^V_{nmq'}\xi^{V*}_{nmq''}-\xi^B_{nmq'}\xi^{B*}_{nmq''})\ , \tag{24}$$

$$\|\mathbf{A}_0\|^2\frac{\partial}{\partial t}j_0=E_0-\eta j_0+\eta\sum_q\alpha_q\lambda^2_{00q}\xi^B_{00q}+\sum_{n,m,q}\frac{ik_n}{\lambda_{nmq}}\xi^V_{nmq}\xi^{B*}_{nmq}+\sum_{n,m,q',q''}\mathcal{F}_{nmq'q''}\xi^V_{nmq'}\xi^{B*}_{nmq''}\ . \tag{25}$$

The coupling coefficients $C_{nmq}\left(\begin{smallmatrix}n' & m' & q'\\ n'' & m'' & q''\end{smallmatrix}\right)$, $\mathcal{D}_{nmq'q''}$, and $\mathcal{F}_{nmq'q''}$ are given by

$$C_{nmq}\begin{bmatrix}n' & m' & q'\\ n'' & m'' & q''\end{bmatrix}=\frac{1}{V}\int_V \mathbf{A}_{n'm'q'}\times\mathbf{A}_{n''m''q''}\cdot\mathbf{A}^*_{nmq}d^3x\ , \tag{26}$$

$$\mathcal{D}_{nmq'q''}=\sum_q\alpha_q\lambda_{nmq''}C_{nmq''}\begin{bmatrix}n & m & q'\\ 0 & 0 & q\end{bmatrix}\ , \tag{27}$$

$$\mathcal{F}_{nmq'q''}=\sum_q\alpha_q\lambda_{00q}C_{nmq''}\begin{bmatrix}n & m & q'\\ 0 & 0 & q\end{bmatrix}. \tag{28}$$

In the derivation of Eq. (25), the electromagnetic driving boundary condition

$$\int_0^{L_z}\oint_0^{2\pi}j_z a\,d\varphi\,dz=\frac{2\pi aL_zE_0}{\eta} \tag{29}$$

is used, where the integral is over the surface of the cylinder. Physically, this means that the averaged current density at the wall is fixed at E_0/η. The integrals involved must be evaluated numerically, using a stored table of the numerically-calculated γ_{nmq} and λ_{nmq}. A table of the $C_{nmq}\left(\begin{smallmatrix}n' & m' & q'\\ n'' & m'' & q''\end{smallmatrix}\right)$ is then itself numerically stored. The first two terms of Eq. (24) represent the possibility of an enforced poloidal rotation and a phenomenogical damping of it that are included for completeness; hereafter, both F_0 and ν_0 will be set equal to zero, throughout this paper.

Define the inverse aspect ratio as

$$\alpha^{-1}=\frac{2\pi a}{L_z}=\frac{r_0}{R}\ , \tag{30}$$

where r_0 is the minor radius and R is the major radius of a torus imagined as being approximated by the straight cylinder.

If we renormalize the variables as $\xi^{V\prime}_{nmq}=a^{-1}\xi^V_{nmq}$, $\xi^{B\prime}_{nmq}=a^{-1}\xi^B_{nmq}$, $B_0'=a^{-1}B_0$, $E_0'=a^{-2}E_0$, $\lambda'_{nmq}=\lambda_{nmq}a$, $\gamma'_{nmq}=\gamma_{nmq}a$, $\eta'=a^{-2}\eta$, and $\nu'=a^{-2}\nu$, and hereafter omit the primes, the radial dimension of the cylinder a is eliminated. (In effect, lengths are being measured in units of the minor radius.) Our inverse aspect ratio, for the runs reported here, is $\pi/4$. We have the final set of ordinary differential equations:

$$\frac{\partial}{\partial t}\xi^V_{nmq}=\sum_{n',m',q'}\sum_{n'',m'',q''}\lambda_{n''m''q''}(\tilde{\xi}^V_{n'm'q'}\tilde{\xi}^V_{n''m''q''}-\tilde{\xi}^B_{n'm'q'}\tilde{\xi}^B_{n''m''q''})C_{nmq}\begin{bmatrix}n' & m' & q'\\ n'' & m'' & q''\end{bmatrix}$$
$$+i\left[\frac{m}{2}+\frac{\alpha^{-1}n}{\lambda_{nmq}}\right](j_0\xi^B_{nmq}-\omega_0\xi^V_{nmq})-i\alpha^{-1}nB_0\xi^B_{nmq}-\nu\lambda^2_{nmq}\tilde{\xi}^V_{nmq}\ , \tag{31}$$

$$\frac{\partial}{\partial t}\xi^B_{nmq}=\sum_{n',m',q'}\sum_{n'',m'',q''}\lambda_{nmq}\tilde{\xi}^V_{n'm'q'}\tilde{\xi}^B_{n''m''q''}C_{nmq}\begin{bmatrix}n' & m' & q'\\ n'' & m'' & q''\end{bmatrix}+\frac{im}{2}(j_0\xi^V_{nmq}-\omega_0\xi^B_{nmq})-i\alpha^{-1}nB_0\xi^V_{nmq}-\eta\lambda^2_{nmq}\tilde{\xi}^B_{nmq}\ , \tag{32}$$

$$a_0\frac{\partial}{\partial t}\omega_0=\nu\sum_q\alpha_q\lambda^2_{00q}\tilde{\xi}^V_{00q}+\sum_{n,m,q',q''}\mathcal{D}_{nmq'q''}(\xi^V_{nmq'}\xi^{V*}_{nmq''}-\xi^B_{nmq'}\xi^{B*}_{nmq''})\ , \tag{33}$$

$$a_0\frac{\partial}{\partial t}j_0=E_0-\eta j_0+\eta\sum_q\alpha_q\lambda^2_{00q}\tilde{\xi}^B_{00q}+\sum_{n,m,q}\frac{i\alpha^{-1}n}{\lambda_{nmq}}\xi^V_{nmq}\xi^{B*}_{nmq}+\sum_{n,m,q',q''}\mathcal{F}_{nmq'q''}\xi^V_{nmq'}\xi^{B*}_{nmq''}\ , \tag{34}$$

where

$$a_0=\frac{1}{8}-\sum_{\gamma_q}\frac{1}{\gamma^2_{00q}}\ . \tag{35}$$

Equations (32)–(35) are solved numerically by using a variable step length, implicit Adams method. For some cases where the system is numerically stiff, Gear's method is used [14]. Since there is no fast-Fourier-transform-like fast algorithm for the Bessel transform, the three-dimensional convolutions appearing in Eqs. (31)–(35) are evaluated directly. For a case with 320 complex modes and 10 real axisymmetric modes (1302 degrees of freedom), it requires 3.7 sec to evaluate the right-hand side of the equations above and the code typically requires 500 sec per poloidal Alfvén time on a Cray-2 for a laminar (nonturbulent) case.

The code is tested for the ideal case in which $\eta=\nu=0$, and no external voltage, in an attempt to determine its accuracy. As expected, both the total energy and the cross helicity are conserved up to rounding error. ($dE/dt, dH_c/dt \le 10^{-12}$ on a Cray-2, where E and H_c stand for total energy and cross helicity, respectively.) Both E and H_c are conserved to the order of one part in 10^7 within 5 Alfvén times with the error tolerance of the ordinary differential equation (ODE) solver set at 10^{-4}.

The results of the numerical solution are also compared with those of the linear instability theory [4,7] for the uniform current density state, which predicts that for the particular set of parameters $\eta=\nu=0.045$ and $B_0=4.5$, when the driving electric field E_0 is increased above 0.33, the mode with $m=1$, $n=1$, $q=1$ becomes unstable first, and its amplitude has a growth rate of 0.279 when $E_0=0.35$. At the same set of η, ν, and B_0, the results of the computation, starting from a low level of initial random noise, show that this $m=1$, $n=1$ mode does start to grow out of the initial random noise at a constant growth rate in the early stage immediately after the driving electric field is raised above the instability threshold predicted by the linear instability theory. A least-squares fitting gives the growth rate of the kinetic energy as 0.555, corresponding to a growth rate of 0.277 in amplitude. This will be displayed graphically in Sec. III.

It will be noted that Eq. (33) has been written with the possibility of a nonzero, volume-averaged, axial vorticity $\omega_0=\omega_0(t)$. This would be important in an application (with an imposed poloidal rotation, for example) in which a net vorticity flux was expected. Rather than set $\omega_0=0$ and discard Eq. (33), however, we compute ω_0 at each time step and monitor its closeness to zero as an additional accuracy check. We find that it hovers about zero with typical excursions of the order of approximately 10^{-4}. The electromagnetic analog, Eq. (34), is of course quite important, governing the net axial current response to the applied electric field; E_0, unlike F_0, has not been chosen to be zero.

As the number of axisymmetric modes retained ($q_{\max}\to\infty$) becomes large, a_0 as given by Eq. (35) becomes small. The coefficients of the time derivatives in such equations as Eq. (34) become small, which necessitates smaller time steps in the (Adams-Moulton) ODE solver with which Eqs. (31)–(34) are time advanced. This results, in practice, in a relatively unrestrictive limitation to moderate values of $q_{\max}$ (the smallest a_0 ever becomes in the computations reported is about 0.0176, for $q_{\max}=10$). The test of the satisfactoriness of the approximation depends upon the existence of a range of $q_{\max}$, corresponding to computable values of a_0, within which the answers become insensitive to further increases in $q_{\max}$. We have established the existence of such ranges in all the computational regimes discussed except the extreme case $\Theta_0\cong 12.34$ ($\Theta\cong 4.8$), where doubts are later expressed about the adequacy of the resolution. We also discuss, in the Appendix, the rather interesting transition behavior in Eq. (34) between a differential equation for $j_0(t)$ and what becomes an essentially algebraic determination of it as a_0 becomes small, in an analytically soluble case.

Equations (31) and (32) are in effect the equations of motion of a large number of driven, nonlinearly interacting, coupled harmonic oscillators with damping. These "oscillators" may, of course, be linearly unstable. The principal numerical difficulty, aside from the task of managing the large arrays, is the computation and storage of the coupling coefficients and the eigenvalues

λ_{nmq}. Once computed and stored for a particular inverse aspect ratio α, this does not have to be done again.

III. RESULTS OF THE DRIVEN SOLUTIONS

A. Helical state formation

At fixed values of B_0, η, and ν, and for given cylinder dimensions, the axial electric field at the wall may be increased from zero. In the laboratory situation, the electric field $E_0(t)$ evolves temporally as part of the dynamics of a circuit of which the plasma is but one element. Here, we assume that $E_0=E_0(t)$ can be programmed to follow any desired time history. In the future, it is intended to embed the present MHD code inside a large one that includes the dynamics of an external circuit.

For small enough E_0, and E_0 constant, the *only* steady state in the presence of uniform η is the zero-flow, axisymmetric state with a current density of only a single component $j_z=E_0/\eta$: the "copper wire" solution. As E_0 is raised incrementally, j_z follows along as fast as the finite resistivity will allow. Since the effect of a changed $E_0(t)$ is felt first at the wall $r=a$, the current profile has to redistribute itself as a function of radius each time. This occurs according to the scenario described in the Appendix.

If we continue to raise E_0, j_z crosses an analytically calculable [7] linear stability threshold at which the uniform current profile becomes unstable. At this threshold, the resistive equilibrium bifurcates, and helically deformed steady states first become possible. Immediately above the threshold, they are characterized by a pair of poloidal and toroidal (axial) mode numbers (m,n) that are the same as those for the first unstable normal mode. The corresponding helical eigenfunctions *are* the first-order parts of the helically deformed equilibria with flow [4].

As we continue to raise E_0, the conditions for the validity of the helical equilibria (so far only calculable as a perturbation series) gradually cease to apply. It appears that there exists a finite range of E_0 between the critical value at which a helical mode becomes unstable and a second critical value, in which the preferred state of the magnetofluid remains a helically deformed steady state dominated by a single pair of (m,n) numbers and eventually, their higher harmonics $(2m,2n)$, $(3m,3n)$, etc. The other modes damp exponentially to zero.

TABLE I. Final states of three runs with different selections of modes, $E_0=0.5$, $B_0=4.5$, $\eta=\nu=0.045$.

	Run 1		Run2		Run3	
m,n,q	E_b	E_k	E_b	E_k	E_b	E_k
0,0,1	0.113 688 782	0.000 000 000	0.113 808 081	0.000 000 000	0.113 810 286	0.000 000 000
0,0,2	0.006 613 172	0.000 000 000	0.006 629 716	0.000 000 000	0.006 629 306	0.000 000 000
0,0,3	0.000 007 651	0.000 000 000	0.000 007 753	0.000 000 000	0.000 007 743	0.000 000 000
0,0,4	0.000 000 228	0.000 000 000	0.000 000 316	0.000 000 000	0.000 000 318	0.000 000 000
0,0,5	0.000 122 740	0.000 000 000	0.000 117 477	0.000 000 000	0.000 117 445	0.000 000 000
0,0,6	0.000 000 710	0.000 000 000	0.000 001 079	0.000 000 000	0.000 001 082	0.000 000 000
0,0,7	0.000 020 481	0.000 000 000	0.000 021 575	0.000 000 000	0.000 021 562	0.000 000 000
0,0,8	0.000 000 093	0.000 000 000	0.000 000 199	0.000 000 000	0.000 000 198	0.000 000 000
0,0,9	0.000 002 962	0.000 000 000	0.000 002 960	0.000 000 000	0.000 002 954	0.000 000 000
0,0,10	0.000 000 146	0.000 000 000	0.000 000 149	0.000 000 000	0.000 000 147	0.000 000 000
0,0,11	0.000 000 707	0.000 000 000				
0,0,12	0.000 000 069	0.000 000 000				
1,1,1	0.073 518 276	0.037 009 276	0.073 520 079	0.037 051 175	0.073 521 048	0.037 050 892
1,1,2	0.001 233 361	0.001 981 446	0.001 236 177	0.001 985 072	0.001 236 184	0.001 985 040
1,1,3	0.002 716 965	0.000 768 223	0.002 722 576	0.000 773 606	0.002 722 605	0.000 773 607
1,1,4	0.000 043 891	0.000 025 060	0.000 042 292	0.000 025 234	0.000 042 292	0.000 025 234
1,1,5	0.000 058 493	0.000 011 624	0.000 058 521	0.000 012 455	0.000 058 522	0.000 012 456
1,1,6	0.000 000 326	0.000 000 071				
1,1,7	0.000 001 544	0.000 000 139				
1,1,8	0.000 000 002	0.000 000 013				
2,2,1	0.005 231 928	0.001 632 140	0.005 263 352	0.001 636 566	0.005 263 267	0.001 636 535
2,2,2	0.000 030 903	0.000 016 356	0.000 031 657	0.000 016 473	0.000 031 657	0.000 016 473
2,2,3	0.000 096 785	0.000 020 867	0.000 099 439	0.000 019 370	0.000 099 437	0.000 019 370
2,2,4	0.000 000 989	0.000 000 174	0.000 000 858	0.000 000 437	0.000 000 858	0.000 000 437
2,2,5	0.000 000 178	0.000 000 757				
3,3,1	0.000 322 734	0.000 037 968	0.000 331 946	0.000 040 347	0.000 331 936	0.000 040 346
3,3,2	0.000 000 197	0.000 000 488	0.000 000 311	0.000 000 595	0.000 000 311	0.000 000 595
3,3,3	0.000 000 156	0.000 006 562	0.000 000 615	0.000 006 224	0.000 000 615	0.000 006 224
3,3,4	0.000 000 012	0.000 000 006				
4,4,1	0.000 013 493	0.000 000 000	0.000 013 526	0.000 000 034	0.000 013 525	0.000 000 034
4,4,2	0.000 000 013	0.000 000 221	0.000 000 009	0.000 000 189	0.000 000 009	0.000 000 189
5,5,1	0.000 000 000	0.000 000 000	0.000 000 668	0.000 000 017	0.000 000 668	0.000 000 017

We have performed several tests of the required resolution as applied to the laminar helical states. A typical example consists of running the same problem with different numbers of retained helical and axisymmetric modes. The results of such a test are shown in Table I, which exhibits, in order, the energetically largest modal energies, for a particular situation. The situation is $E_0=0.5$ ($\Theta_0=1.23$), 40 Alfvén units after it is set at that value. The other parameters are the same as in Secs. III A and III B ($\eta=\nu=0.045$, $B_0=4.5$, etc.). Shown are the results of retaining 455 modes (443 helical and twelve $00q$ modes, "Run 1"), 330 modes (320 helical and ten $00q$ modes, "Run 2"), and 25 modes (15 helical and ten $00q$ modes, "Run 3"). Displayed are the m,n,q values and the magnetic energy E_b and kinetic E_k returned by the computation. It will be seen that while minor discrepancies result between the 25 mode and 330 mode runs, the differences between the 330-mode treatment and the 443-mode treatment are entirely negligible.

We also address, in the Appendix, an interesting related mathematical point raised: namely, what happens to the computational scheme for very large $q_{\max}$, as a_0 in Eqs. (32) and (34) becomes small.

As E_0 is raised past a second critical value, we finally observe transitions from a state dominated by one pair of (m,n) numbers to another laminar state involving many modes. One distinct feature of the latter is that all the modes included in the calculation participate in the final state and form a broadband energy spectrum. None of them decays to zero as those modes other than the dominant one and its harmonics do in the final state at a lower E_0. All the modes are stationary in time except for some small oscillations of the high wave-number modes with low energy, at the noise level. We describe presently a reproducible transition from (1,1) to a multimode state with $(m,n)=(1,2)$ and (3,4) as the two biggest modes, for example. The reason for these transitions is not entirely clear, but the evidence we have is consistent with a minimum rate of energy dissipation as being the basis for selection among competing helical states with different mode numbers, at successive bifurcations.

Figure 1 is taken from the time development of a run in which the E_0 field is raised quasiadiabatically from zero in small steps. Shown is only the step at which E_0/η crosses the stability boundary (indicated by the dashed horizontal line in Fig. 1) for the first time. This run is for the parameter set $B_0=4.5$, $\eta=\nu=0.045$ (so that $S=H=100$), and $\alpha^{-1}=\pi/4$. The dashed curve is the axial current $j_0(t)$, which is following E_0, and by about $t=20$ (times are always in poloidal Alfvén transit times), $j_0(t)$ has adjusted itself to the value $E_0/\eta=0.35/0.045\cong 7.78$. The dotted curve (which, because of the close spacing of the dots, appears to become a solid curve after about $t=10$) is the total kinetic energy (the scale is on the right of the graph), which is decaying from initial broadband random noise deliberately distributed among the modes. For the computation shown in Fig. 1, there are 330 independent modes present, includ-

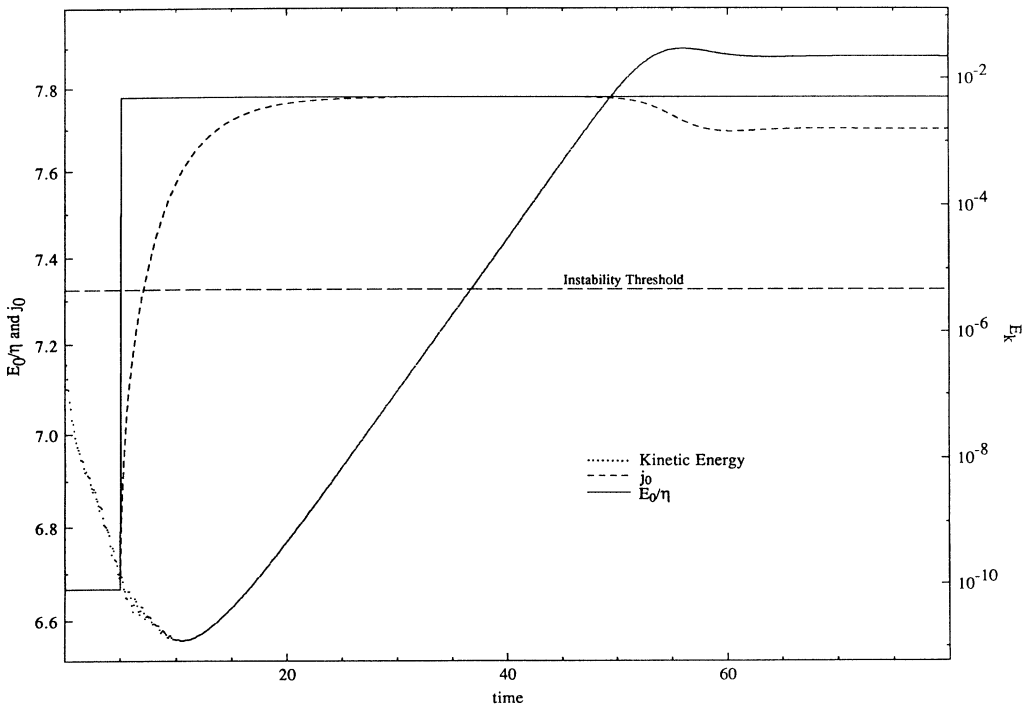

FIG. 1. Time history of total current (dashed curve), total kinetic energy (dotted curve, the later stages of which appear solid), and applied electric field (solid step), plotted vs t in poloidal Alfvén transit times. For this step in the electric field, the current crosses, between $t=5$ and 10, the threshold for the appearance of the first linearly unstable mode. The dashed horizontal line is the current threshold.

ing all those with $\lambda^2_{nmq} < 100$ for m and n not both zero. The $00q$ modes, up to $q=10$, are required for the development of the radial variation in the current and magnetic field.

As the current density j_0 approaches its new uniform value above the threshold just before $t=20$, the kinetic energy begins to grow exponentially at a rate numerically measured to be 0.555, compared with a theoretical value of 0.558; this is thought to be satisfactory agreement. E_0 is held at this constant (supercritical) value and the kinetic energy ceases to grow at about $t=50$. By $t=60$, it has approached a constant value and there has been an accompanying depression of $j_0(t)$ to a constant value below E_0/η. All quantities become time independent and this saturated state with flow will apparently persist indefinitely.

Figure 2 shows the time histories of the largest nonaxisymmetric modal kinetic energies (i.e., those with m and n not both zero). Since the plot is logarithmic, it will be seen that for all practical purposes, the helical part of the final state is characterized by only a single Chandrasekhar-Kendall function and it is the $\mathbf{A}_{111}$ mode ($m=1$, $n=1$, $q=1$). Inspection of the corresponding plot for the nonaxisymmetric magnetic modal energies reveals the same dominance of the energy spectrum by the (1,1,1) mode. Notice that the majority of the modes simply damp away in about ten Alfvén times. The single-mode, perturbation-theoretic, helical equilibrium [4] appears to be adequate to characterize the region immediately above the stability threshold.

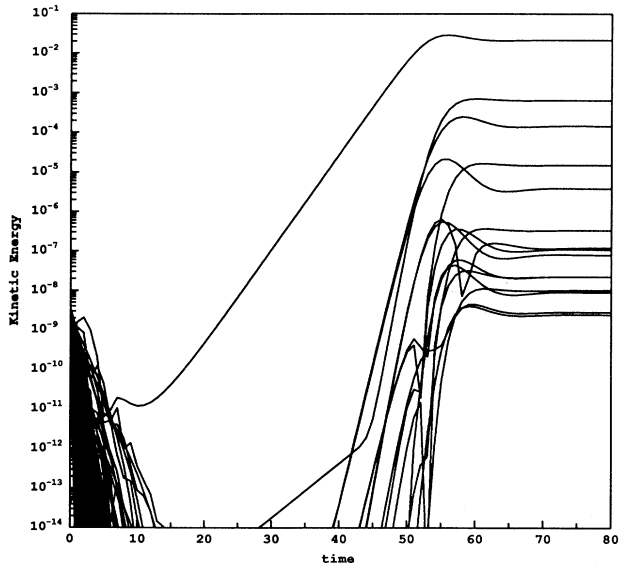

FIG. 2. Time histories of the largest helical modes in the kinetic energy for the same situation as shown in Fig. 1. Note that a time-independent laminar state has been achieved by about $t=65$. The dominant mode has $(m,n)=(1,1)$, and second most dominant mode, down by over an order of magnitude, has $(m,n)=(2,2)$.

In another set of circumstances, the (1,1) amplitudes were artificially set equal to zero after the (1,1) state had become dominant ($E_0=0.35$), in the manner of Cappello and Paccagnella [15], who have speculated that the previously dominant mode, once removed, might remain absent. However, in our case, removal of the (1,1) state at $t=80$ was followed by its regrowth and eventual dominance by $t\cong 125$.

Figure 3 shows $j_z(r)$, $B_z(r)$, $j_\varphi(r)$, and $B_\varphi(r)$, the axisymmetric parts only of the relevant fields as functions of radius. Except for these modifications of the radial dependence of the axisymmetric parts of the fields, the state is essentially that predicted by the three-mode Galerkin truncation [9]. Both B_z and j_z do not greatly depart from their uniform "copper-wire" value.

Figure 4 shows the time histories of $E_0(t)$ and $j_0(t)$, and the kinetic energy as the electric field is stepped through several increments for the same B_0, η, ν, and α^{-1} as in Figs. 1–3. The helical (1,1,1) state followed along and continued to adjust its contribution. (No additional random noise was added after the time $t=0$.) Somewhat unexpected, however, was the observation that the helical amplitude did not continue to increase, as E_0 was increased, according to the simple predictions of the three-mode truncation [9]. Compensating adjustments in the radial behavior of j_0, B_z, etc., seemed gradually to eliminate this increase predicted by the three-mode truncation, and the state at the end of the sequence shown in Fig. 4 seems to be returning to its axisymmetric copper-wire values.

Figures 5 summarize the steady-state values of j_0 and the total computed dissipation rate, Ohmic plus viscous, as E_0 is increased. The values characteristic of the (1,1,1) state are shown as open circles. As E_0 increases, the departure between the helical state's dissipation and that of the corresponding axisymmetric zero-flow state at first increases and then decreases. The corresponding kinetic energies appear in Fig. 5(c). If one were to look at only the open circles in Fig. 5(b), one might conclude that the axisymmetric, zero-flow equilibrium was again being approached near $E_0=0.6$.

This approach, however, is illusory, because at a lower value of E_0 between 0.5 and 0.55, the helically deformed (1,1,1) state has itself become unstable. If a small but finite amount of broadband noise is introduced, a sudden nonlinear evolution is observed into a *different* laminar helical state involving all the modes included in the calculation. This corresponds to the darkened square in Figs. 5(a) and 5(b), and is seen to be associated with a lower dissipation rate than that for $(m,n)=(1,1)$. This is the first example of a transition between helical steady states, and we do not know at this point how many more such transitions may be expected as E_0 is increased. We have called it the "multimode" state.

A gray-scale spectral plot for the state $(m,n)=(1,1)$ is shown in Fig. 6, again illustrating the single-mode dominance. But now, higher harmonics such as (2,2) are noticeably involved and their prominence is greater than before. Figure 6 is for $E_0=0.35$.

The departure of the MHD configuration from the

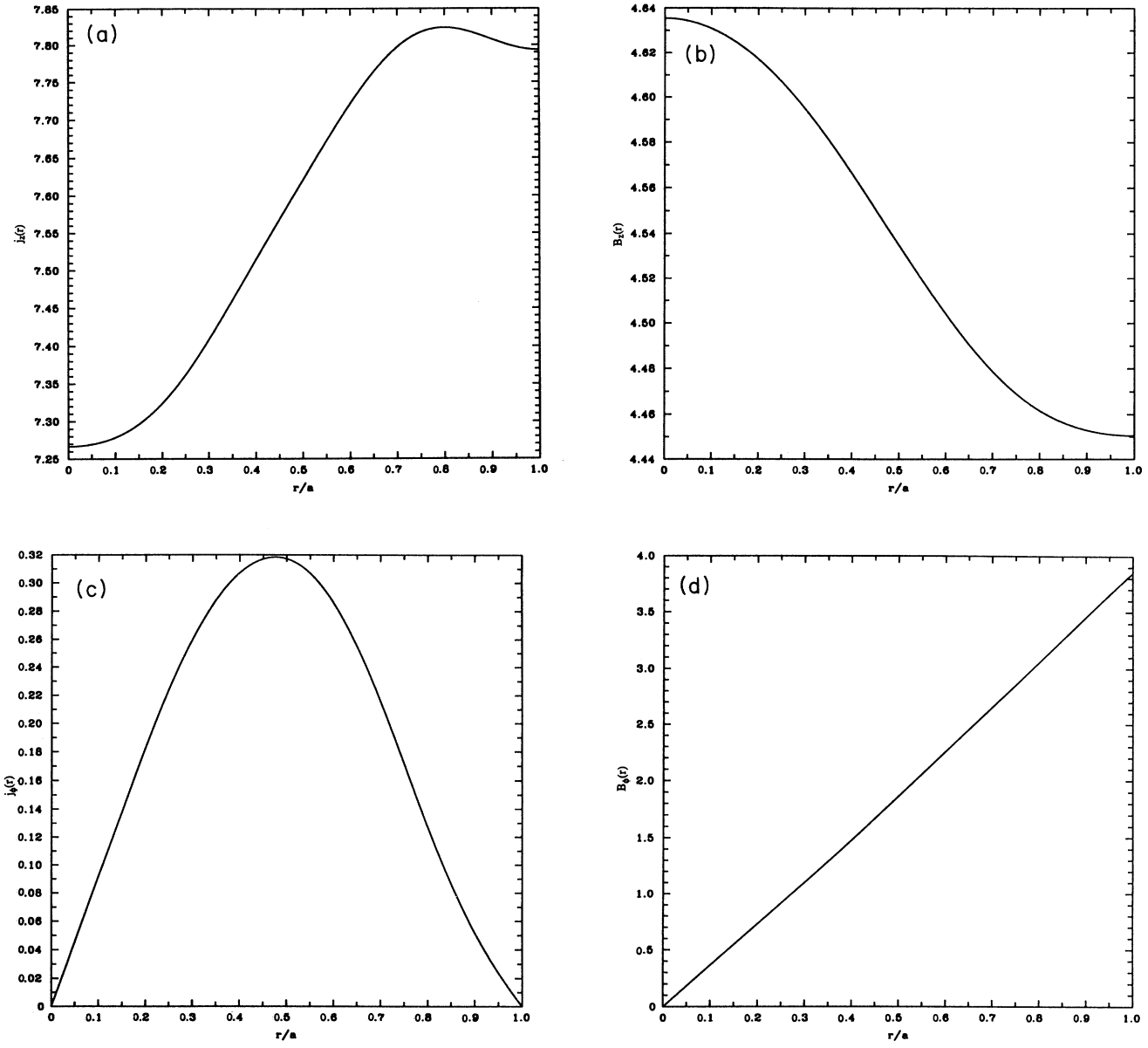

FIG. 3. Radial profiles, at $t=100$, of the axisymmetric parts of the magnetic field and current density for the situation of Figs. 1 and 2: (a) $j_z(r)$; (b) $B_z(r)$; (c) $j_\varphi(r)$; (d) $B_\varphi(r)$. Note that the pinch ratio $\Theta=B_\varphi(a)/\langle B_z\rangle$ is about 0.856, compared with the value $\Theta_0=0.864$ for the axisymmetric zero-flow solution.

(1,1) state, under the addition of random noise at $E_0=0.6$, indicates that some kind of transition to a preferred laminar state other than (1,1) has occurred by this value of $\Theta_0\simeq 1.36$. This is an example of what appears to be a somewhat complicated transition behavior that occurs in this intermediate range of Θ_0, well before anything that could be called true MHD turbulence develops. We do not explore this transition behavior in detail in this article. We may offer, however, a few additional observations about the regime around $E_0=0.55$, $\Theta_0\simeq 1.36$ before passing to an example of a fully turbulent state for the high values of Θ_0.

B. Transition between helical states

Shown in Fig. 7(a) is a plot of the evolving kinetic energy with individual helical modal contributions shown separately. Initially $E_0=0.5$ ($\Theta_0=1.23$) and the other parameters are the same as reported above. The system starts from the unstable axisymmetric equilibrium with a small amount of random noise (at the level of approximately 10^{-8} in energy). In the earliest stage ($t<10$), several linearly unstable modes start to grow out of the initial random noise, while the majority of the modes damp away as predicted by the linear theory [4,7]. As

soon as the energies of these helical modes get to a level where the linear theory ceases to apply, the system undergoes a complicated nonlinear transient process and finally, after $t \cong 30$, a stationary final state similar to that which appeared in Fig. 6 is formed with the dominant (1,1) mode and its harmonics (cf. Table I). The other modes keep damping exponentially.

At $t=60$ the driving electric field E_0 is stepped up from 0.5 to 0.55. The previously dominant modes adjust their amplitudes to a new level, while all the other modes

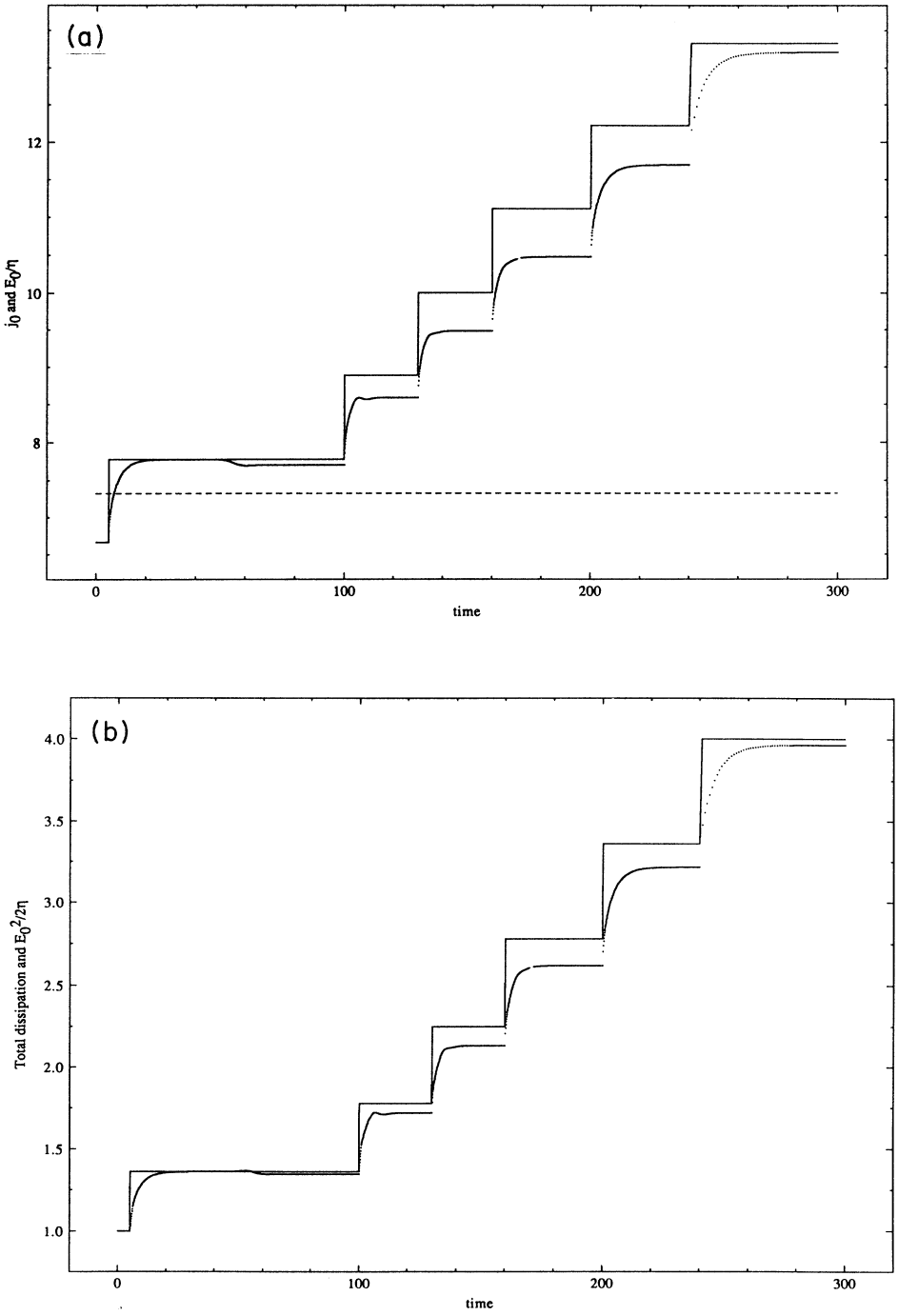

FIG. 4. (a) Total current and (b) total energy-dissipation rate for the continuation of the run shown in Figs. 1–3. The square steps in (a) are the electric field E_0, which is being gradually raised; the steps in (b) are the Ohmic dissipation for the associated "copper-wire" solution without flow, and the lower curve is the measured total dissipation. The flat dashed line in (a) is the threshold current. Note the significant *decrease* in the gaps between the computed and zero-flow quantities at the last steps, just below $t=300$.

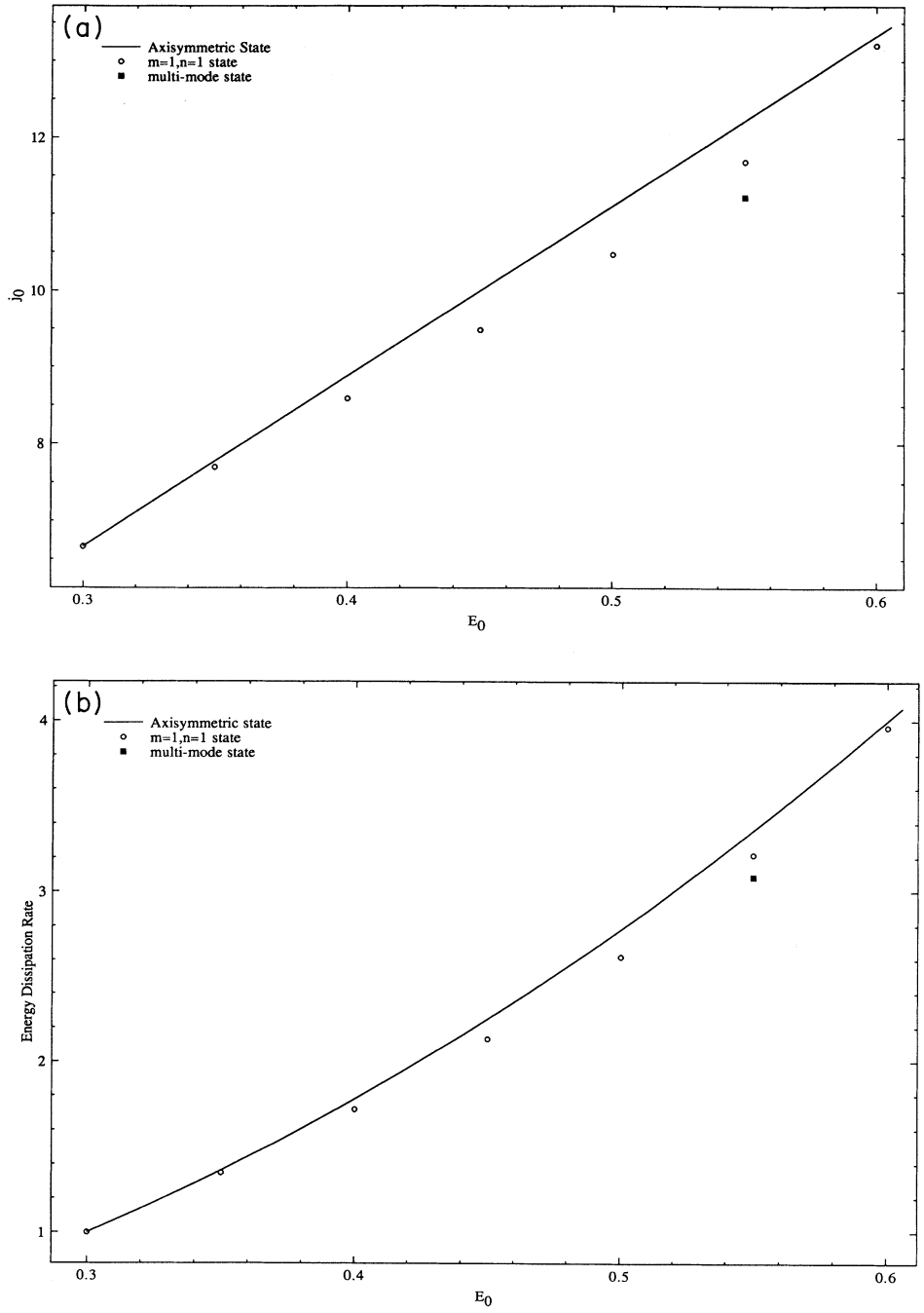

FIG. 5. (a) Time-averaged total current and (b) total energy-dissipation rate for the series of electric-field strengths between 0.35 and 0.6 shown in Fig. 4. The helical state with $(m=1, n=1)$ follows along (open circles), with increasing E_0, but by $E_0=0.55$, has become unstable to the addition of a small amount of random noise. If noise is added at the energy level 10^{-8} at $t \cong 300$, an abrupt transition to a laminar helically deformed multimode state is observed; the new state is indicated in Figs. 5(a) and 5(b) by the blackened square at $E_0=0.55$. In Fig. 5(c), kinetic energy and magnetic energy for the successive (1,1) states are shown. The cross and square indicate, respectively, the kinetic and magnetic energy for the multimode state that the $E_0=0.55$ (1,1) state may be perturbed into.

start to grow exponentially, and after another complicated nonlinear process, only the dominant part of which is shown, in Fig. 7(a), a new stationary final state, is reached again. But this time, the final state is *not* dominated by a single pair of (m,n). Instead, a broadband energy spectrum is formed with the two largest modes identified as (1,2) and (3,4). The energies of all the other modes included in this calculation are maintained at a low but

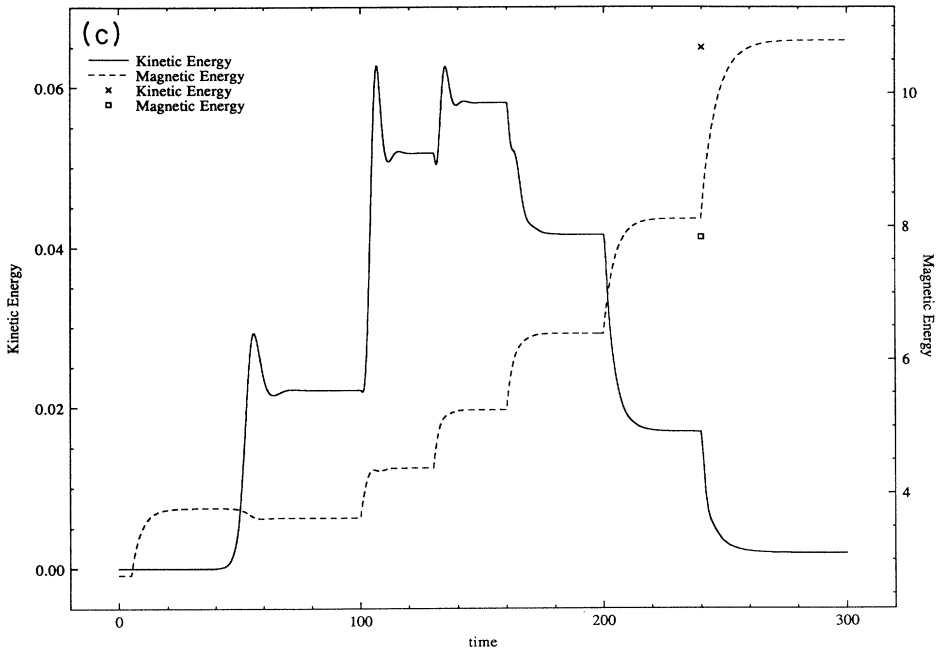

FIG. 5. (*Continued*).

constant level, which is a distinction from the previous stationary state reached at $t=60$. Small oscillations can be observed at a very low energy level.

A gray-scale spectral plot in Fig. 7(b) at $t=160$ reveals that there is an approximate preferred direction in the m,n space along which the modes are excited. (This preference of direction is observed in several different selections of modes corresponding to other runs in addition to what is shown in Fig. 6.) The modes with an even n number appear to contain most of the energy.

Since this set of modes is originally selected for a different case, it does not fit the preferred direction very well. To improve the resolution, a new set of modes is selected to fit the preferred direction in Fig. 7(b) better, and the final state at $t=160$ is used as the initial condition to start a new calculation. The modal kinetic-energy plot and a gray-scale spectral plot for this new calculation at $t=20$ are shown in Figs. 7(c) and 7(d). The negligible difference, except for those modes which had not been previously included, of the two calculations with different selections of modes may indicate the adequacy of spatial resolution.

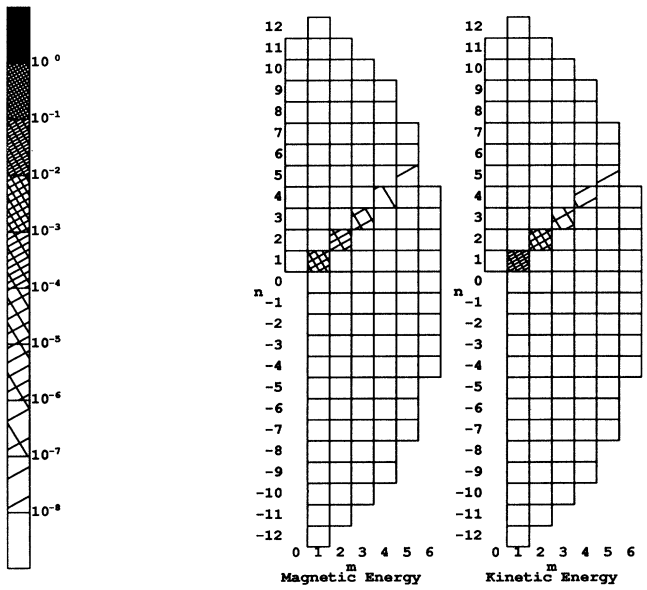

FIG. 6. "Gray-scale" spectral density plot, in (m,n) modal space, for the helical (1,1) state at $t=80$ (see Figs. 1 and 2). Only $(m,n)=(1,1)$ and its first three harmonics are seen to be participating noticeably in the nonaxisymmetric part of the spectrum.

C. A fully turbulent state

The parameter space to be explored is large and we make no attempt at a comprehensive search here. For $B_0=4.5$ and $\eta,\nu=0.045$ (Lundquist and Hartmann numbers of 100) we have explored the region between $E_0=0$ and 1 (pinch ratio for the axisymmetric state $\Theta_0\cong 2.5$, actual computed pinch ratio $\Theta\cong 1.9$) rather carefully, and have found only the laminar helical states, above the stability threshold, that have been described in Secs. III A and III B. [$B_z(a)$ had not yet reversed sign at $\Theta\cong 1.9$.] In this subsection, we describe the results of a computation with η, ν, and B_0 the same, but with $E_0=5.0$. A fully developed turbulent state with observed pinch ratio $\Theta\cong 4.8$, considerably less than the equivalent zero-flow

axisymmetric value ($\Theta_0 \cong 12.34$) is observed. Between these values of Θ_0 (2.0 to 12) or E_0 (1.0 to 5.0) for these values of ν, η, there is a complex transition to fully developed MHD turbulence. We leave the detailed exploration of this transition to the future; it may be expected to occur across a generally rising curve in a plane whose axes are inverse Hartmann number squared and axisymmetric pinch ratio Θ_0, shown in Fig. 8. The "tokamak regime" will roughly correspond to the lower left-hand part of the curve and the "reversed-field pinch (RFP) regime" will lie above it and to the right. From the point of view of incompressible MHD, the two regimes can be located in the same (Θ_0, H^{-2}) plane.

Figure 9 is a plot that combines the values of j_0 and dissipation rate achieved for those runs with $E_0 \leq 1.0$ and the one with $E_0 = 5.0$. The $E_0 = 5.0$ state is highly turbulent, and a time average is required to achieve the values plotted. Figure 10 is a time history of $j_0(t)$ and a

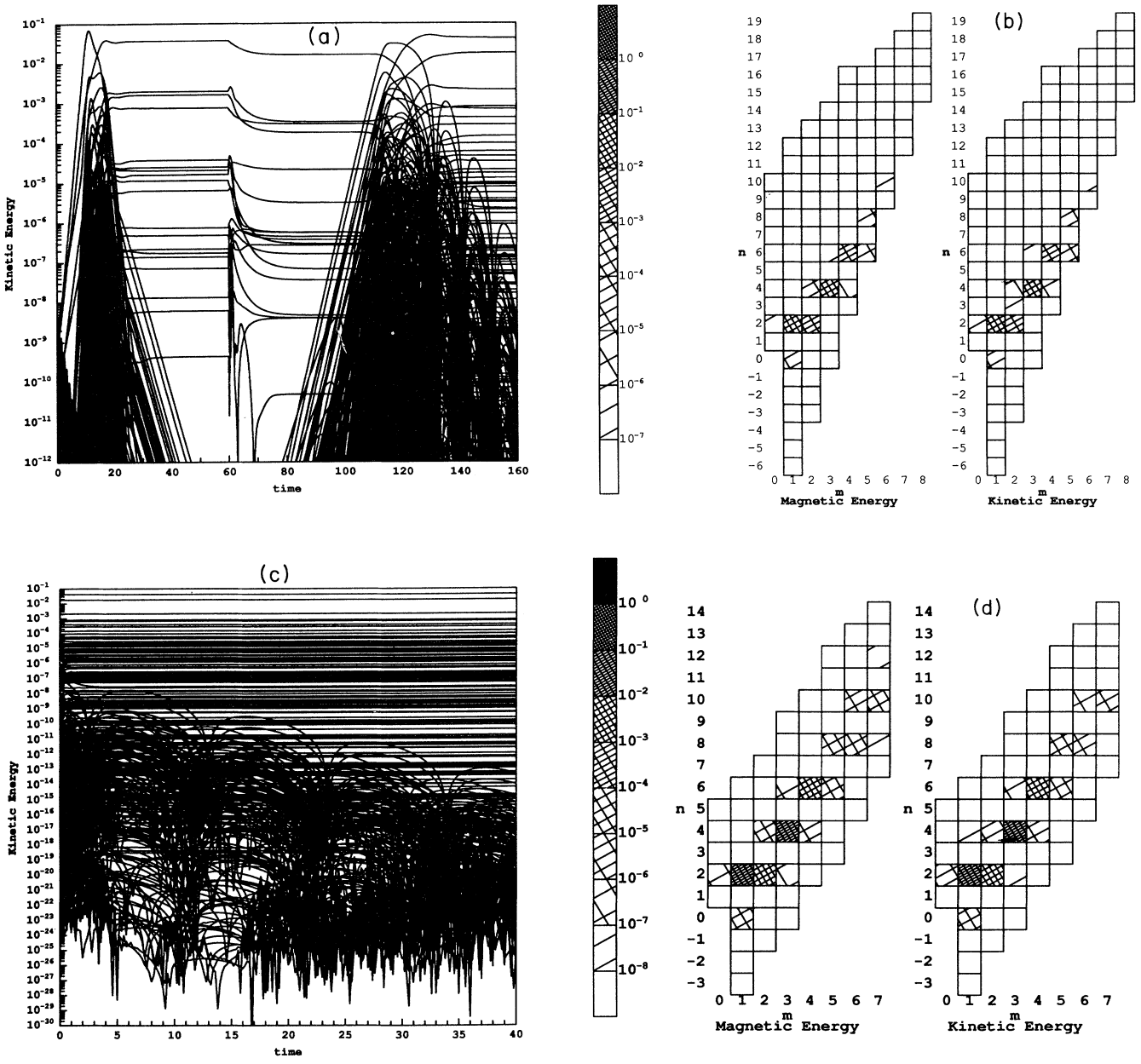

FIG. 7. (a) Evolving kinetic modal energies, starting from a flat-current profile ($j_0 = E_0/\eta$) plus broadly distributed random noise. E_0 is raised from 0.5 to 0.55 at $t = 60$. (b) Gray-scale spectral plot at $t = 160$ shows that (1,2) and (3,4) are the two biggest modes. The final state of (a) is used as the initial condition to start a new better resolved calculation presented in (c), the time histories of modal kinetic energies, and (d), a spectral plot at $t = 20$ units after restarting the run with a more appropriate set of (m,n) modes retained.

total dissipation rate for the $E_0=5.0$ run. A modal history of the helical kinetic-energy amplitudes is shown in Fig. 11, where the turbulence is apparent. It is equally apparent in Fig. 12, which is a gray-scale modal energy plot of the (m,n) energy spectrum for the velocity field and magnetic field. The computed Kolmogoroff dissipation wave number is $K_0 \cong 33$, which is to be compared with the maximum allowed λ_{nmq} of 10. A larger modal

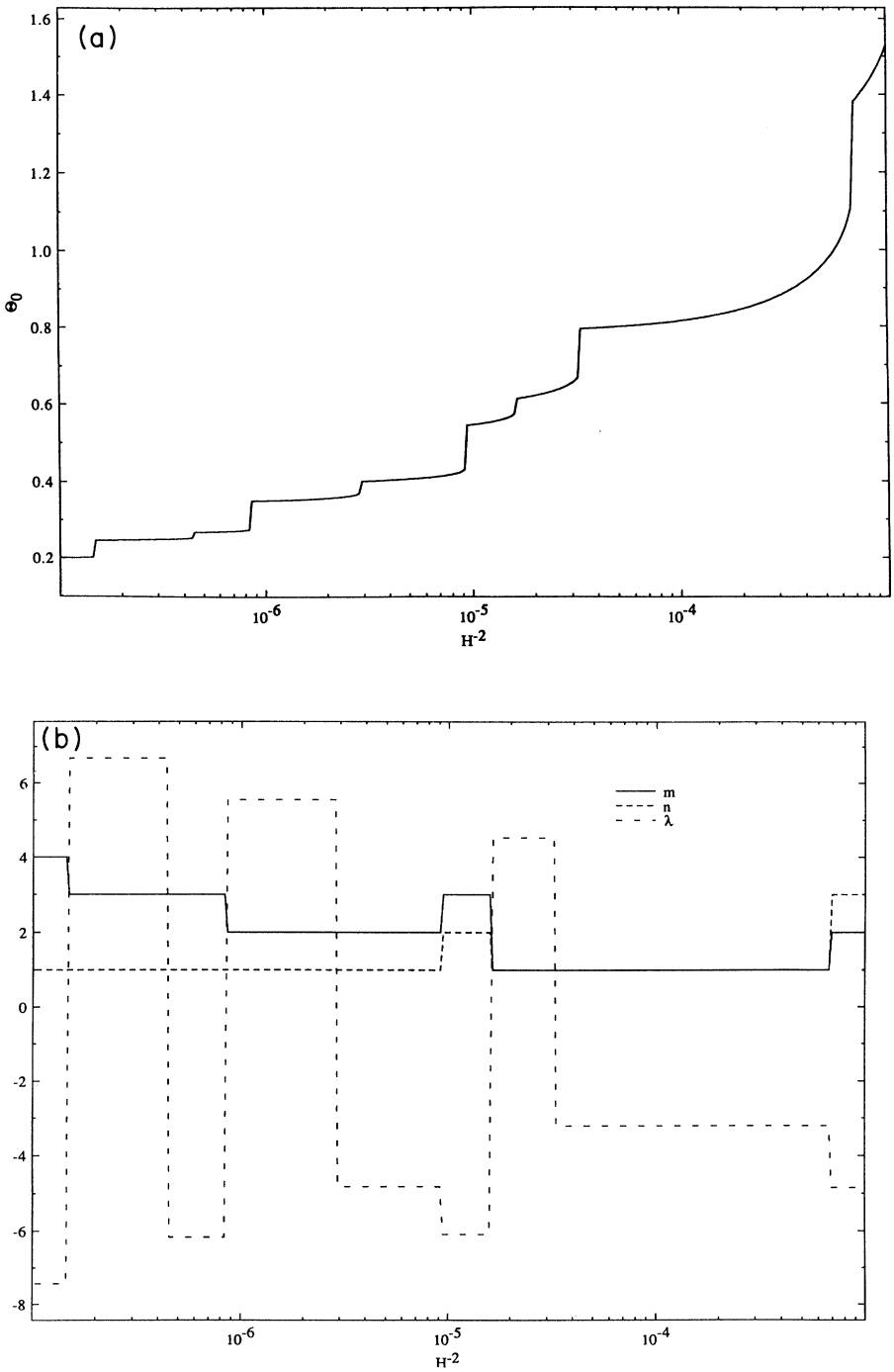

FIG. 8. (a) Threshold curve above which the axisymmetric, zero-flow current profile is unstable and above which are expected, at first, laminar helical states, and then MHD turbulence ($B_0=4.5$, $\eta=\nu=0.045$, $a=1$, $\alpha^{-1}=\pi/4$). Axisymmetric zero-flow pinch ratio Θ_0 is plotted vs inverse Hartmann number squared. H^{-2} decreases linearly with decreasing $\eta\nu$ and Θ_0 increases with increasing toroidal voltage. (b) Dominant m,n,λ (for the first unstable helical mode as Θ_0 is raised) vs H^{-2} for the situation shown in (a).

space will likely be required to obtain a well-resolved solution for this case. The root-mean-square kinetic wave number may be estimated as the square root of the ratio of enstrophy to kinetic energy, and is approximately equal to 7.23. Large (~ 0.1) excursions of ω_0 about zero also indicate that this run may not be well resolved.

IV. DISCUSSION

It is now possible to formulate with some confidence, and within the limitations of one-fluid incompressible MHD with scalar, uniform transport coefficients, what the regions of qualitatively different behavior are for a

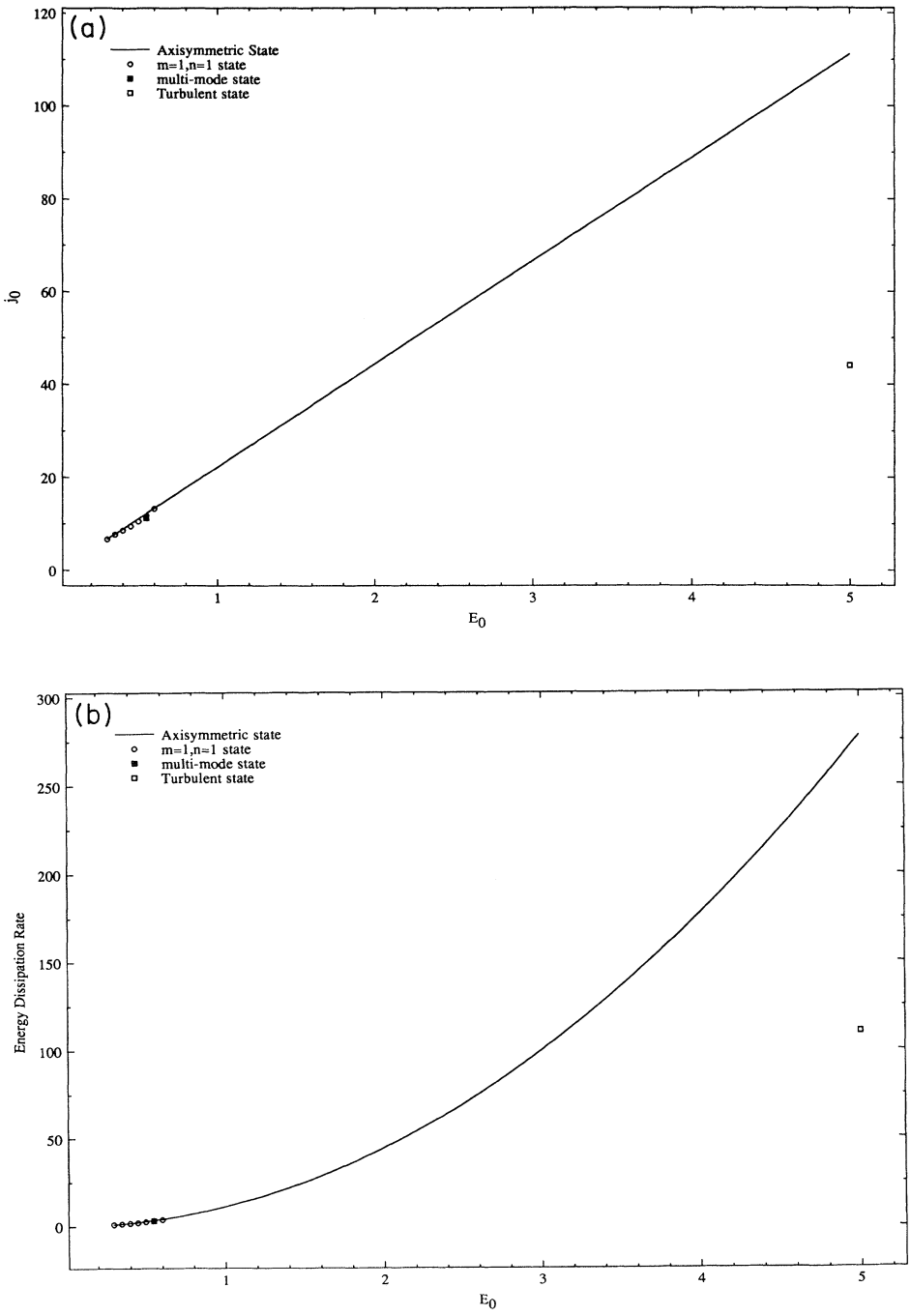

FIG. 9. (a) Time-averaged current and (b) total energy-dissipation rate for $E_0 \leq 1$ and $E_0 = 5$. The state with $E_0 = 5$ is highly turbulent.

periodic cylinder of uniform density magnetofluid, supported by a dc magnetic field $B_0\hat{e}_z$, and driven by a fixed toroidal wall voltage E_0L_z (L_z is the length of the periodic cylinder).

For a given aspect ratio α, there is first of all a quiescent regime for low enough η in which the current profile is flat and there is no flow. This is the relatively uncomplicated regime below the rising curve in Fig. 8(a) (for aspect ratio $\alpha=4/\pi$). As the plasma is driven harder (the quiescent pinch ratio Θ_0 increases) or as the dissipation coefficients decrease (the inverse Hartmann number squared decreases), this stability boundary is always crossed, and the mechanical activity begins.

As the stability boundary is crossed, a lower energy-

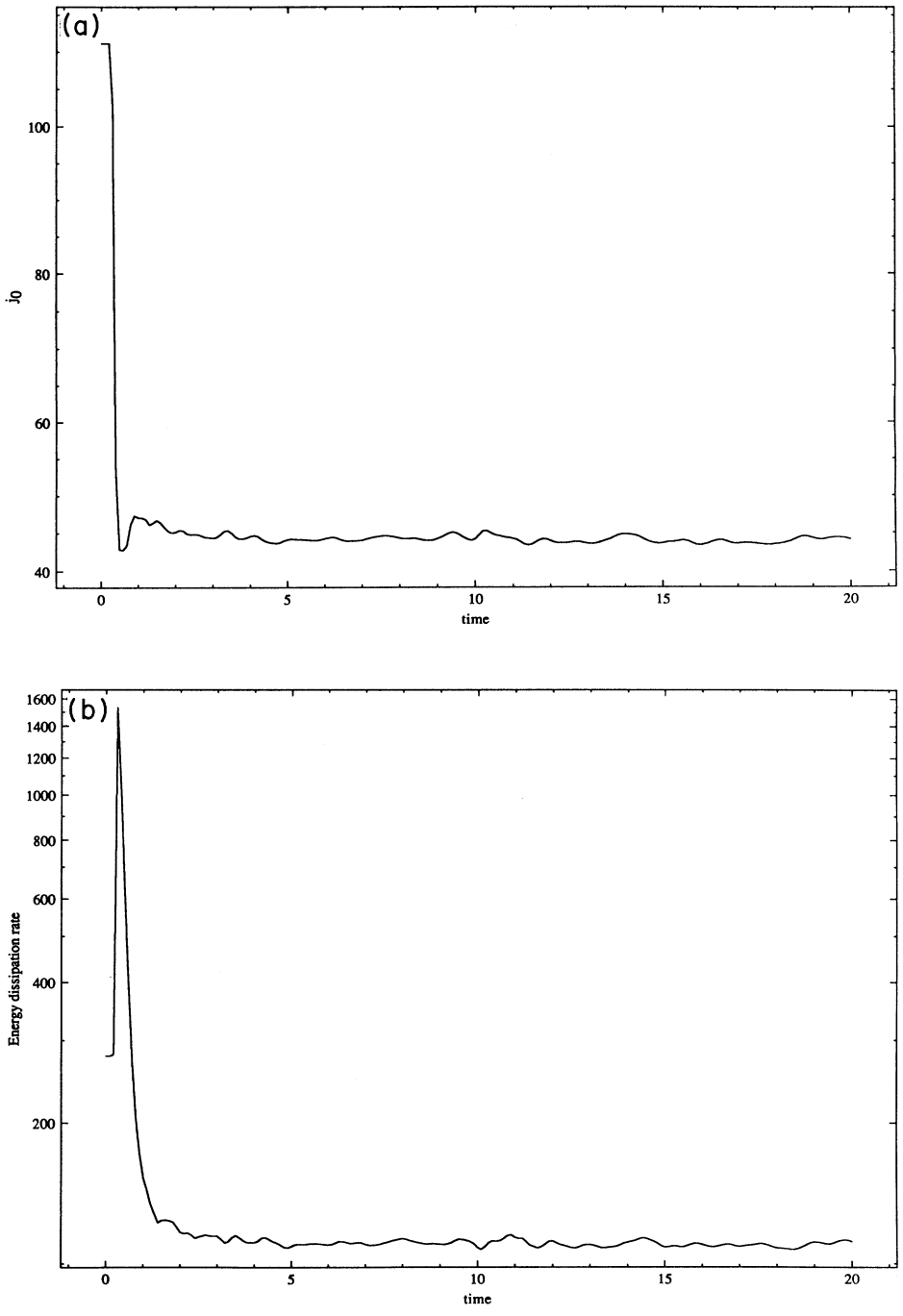

FIG. 10. (a) Time history of total current and (b) total energy-dissipation rate for the turbulent ($E_0=5.0$) run. (Here, $\Theta_0\cong 12$, but $\Theta\cong 4.8$.)

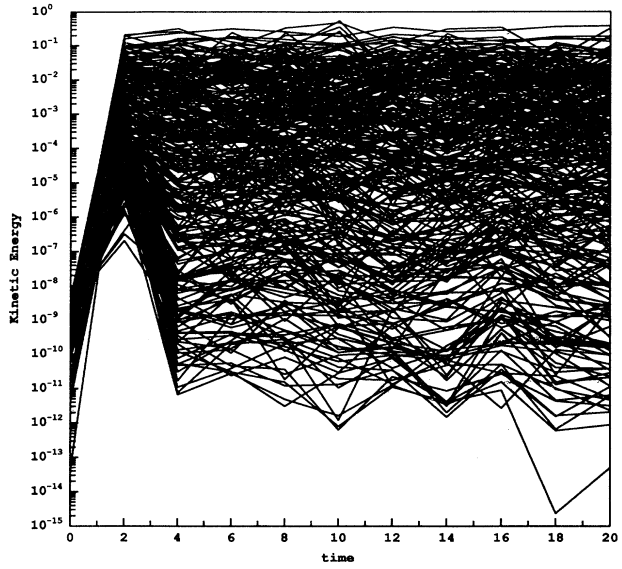

FIG. 11. Modal kinetic-energy history of the $E_0=5.0$ run.

dissipation-rate laminar state forms and is characterized by paired helical vortices and helical distortions of the current channel. There is a single dominant pair of (m,n) mode numbers, which can be read off Fig. 8(b). The analytical perturbation-theory version of the helical state [4] seems to work satisfactorily at and immediately above (in Θ_0) the threshold, but ceases to work as Θ_0 is raised across a second threshold at which the system changes from a single-mode-dominant laminar state to a multimode laminar state. Large contributions from higher $00q$ modes considerably distort the axisymmetric parts of the field profiles. These are unfamiliar, and at this point we do not have a satisfactory analytical representation of them. Nor do we know what other possible transitions among laminar states will be found as the driving voltage is raised.

Eventually, at a third threshold, which we have made no attempt here to quantify, the laminar states containing the steady helical modes give way to what can properly be called a fully developed MHD turbulent state. The present spatial resolution for this strongly driven run ($\Theta_0\cong 12.34$ and $\Theta\cong 4.8$ may be higher than any laboratory values of these parameters ever achieved) seems likely to be inadequate (cf. Fig. 12). Larger numbers of modes need to be employed, and future attention will be given to this problem.

Two immediate problems suggest themselves as natural applications of the code which has been developed: (i) detailed exploration of the transition behavior within the band above the curve where the laminar helical states first appear; and (ii) characterization of the fully turbulent state (spectral distribution, degree of anisotropy, helicity content, level of fluctuations about the mean, etc.), which appears above this supposed band of laminar states.

Longer-range generalizations which seem highly desirable include (i) the inclusion of spatially variable temperature, locally temperature-dependent transport coefficients, and an energy equation; (ii) the inclusion of finite compressibility and nonuniform density; (iii) the embedding of the MHD code within a slightly larger code that includes the effects of the external circuit; and (iv) comparison of the results with several tantalizing experimental hints of persistent helical states in toroidal pinches and tokamaks [16–18]. The largest uncertainty in any detailed application of the theory is perhaps that of knowing what numerical values of the transport and dissipation coefficients to use inside a real confinement device.

It may be unnecessary to reiterate [3,4,9,19] that the helically deformed states computed here are quite distinct from the minimum-energy, or "Taylor," state familiar in the theory of the reversed-field pinch [20]. That state has no flow or vorticity ($v_0=0$) and so cannot satisfy Eq. (2) with nonzero η. It is also the case that the present helical deformations set in at far lower thresholds in Θ than in the "Taylor state," thresholds that are sensitive to values of ν and η.

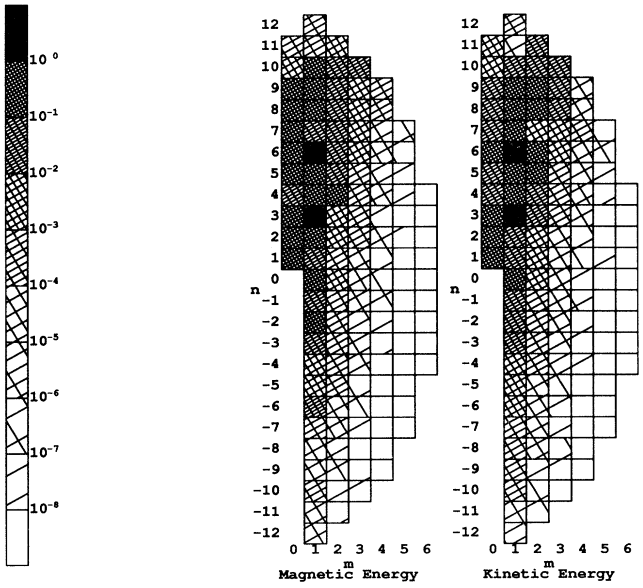

FIG. 12. Gray-scale plot of the modal energies for the fully developed turbulent run with $E_0=5.0$. The fact that significant modal excitation occurs out to the perimeter of the truncated (m,n) space probably indicates inadequate spatial resolution.

ACKNOWLEDGMENTS

This work was supported in part by U.S. Department of Energy Grants Nos. DE-FG02-85ER-53194 and DE-FG02-85ER-53298, and by NASA Grant No. NAG-W-710.

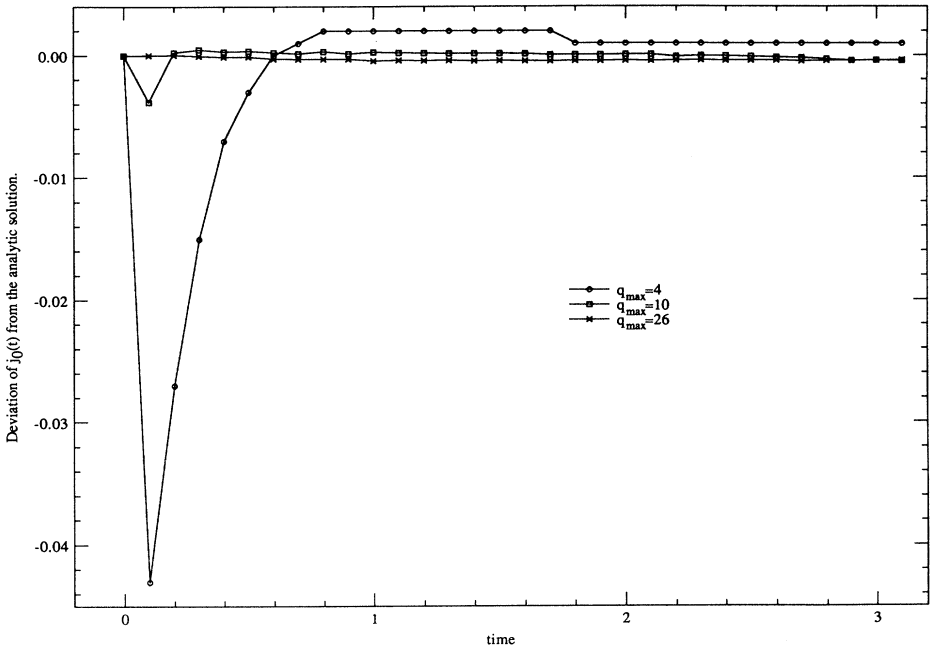

FIG. 13. Deviation of $j_0(t)$ from the analytical solution to the electric-driven, conducting cylinder problem of the Appendix.

APPENDIX

The structure of Eq. (25) or (34) is unusual enough to deserve comment. The norm a_0 of the test function $\mathbf{A}_0$ becomes small as the number of axisymmetric modes retained approaches infinity ($q_{\max}\rightarrow\infty$). In the computation, the decrease of a_0 requires smaller time steps, and these are automatically provided by the ODE solver. In the examples presented, a_0 is never smaller than about 0.0176, so the reduction in time step never appears as a serious problem. The independence of the answer upon $q_{\max}$, as $q_{\max}$ increases, is taken as sufficient justification for the retained number of modes.

It is nevertheless interesting to inquire into the analytic behavior of the system as $q_{\max}\rightarrow\infty$. It is the case that Eq. (34) exhibits behavior that goes over continuously from a differential-equation-like determination of j_0 to an algebraic one, as a_0 becomes smaller and smaller. This behavior can be illustrated by considering a simplified magnetics problem that is a special case of Eqs. (32) and (34).

We consider a rigid ($\mathbf{v}=0$) uniform cylinder of conducting material, initially current free, to which an electric field $E_0\hat{\mathbf{e}}_z$ is impulsively applied at the wall at $t=0$ and thereafter is held constant. The problem is the standard textbook one of an axisymmetric diffusion equation

$$\frac{\partial j_z}{\partial t}=\eta\nabla^2 j_z\ , \tag{A1}$$

where $j_z=0$ for $t<0$, but is suddenly constrained to be j_0 for $t\geq 0$ at $r=a$. Defining $J_z=j_z-j_0$, J_z can be solved for as a series of Bessel functions $J_0(\gamma r)$, where $J_0(\gamma a)=0$ and $J_z=-j_0$ initially. This solution is analytically easy and will hereafter be called the "exact" solution. It can be plotted to any desired accuracy.

From the point of view of the approximate system of Eqs. (32) and (34), we are left with the pair of relations

$$\frac{\partial\xi^B_{00q}}{\partial t}=-\eta\lambda^2_{00q}\tilde{\xi}^B_{00q}=-\eta\lambda^2_{00q}(\xi^B_{00q}-\alpha_q j_0) \tag{A2}$$

and

$$\begin{aligned}a_0\frac{\partial j_0}{\partial t}&=E_0-\eta j_0+\eta\sum_q\alpha_q\lambda^2_{00q}\tilde{\xi}^B_{00q}\\&=E_0-\eta j_0+\eta\sum_q\alpha_q\lambda^2_{00q}(\xi^B_{00q}-\alpha_q j_0)\ .\end{aligned} \tag{A3}$$

Here, q is summed up to $q_{\max}$ and a_0 is $\frac{1}{8}-\sum_q\lambda^{-2}_{00q}$, where the sum again runs up to $q_{\max}$. Both ξ^B_{00q} and j_0 vanish for $t\geq 0$, and E_0 is suddenly raised from zero to a constant value at $t=0$.

The system can be solved analytically, by taking Laplace transforms in time,

$$\int_0^\infty j_0(t)e^{-ts}dt\equiv\mathcal{J}_0(s)\ , \tag{A4}$$

where s is the complex argument of the Laplace transform, and similarly for all time-dependent quantities. Equations (A2) and (A3) are converted into an algebraic system which may be solved at once for $\mathcal{J}_0(s)$ to give

$$\mathcal{J}_0(s)=\frac{E_0}{s\left[sa_0+\eta+\eta s\sum_q^{q_{\max}}\dfrac{\alpha_q^2\lambda^2_{00q}}{s+\eta\lambda^2_{00q}}\right]}\ . \tag{A5}$$

All the poles of Eq. (A5) are real and have $\mathrm{Re}(s)<0$, except for the pole at $s=0$. There are an infinite number, which lie along the negative real axis between the values of $\eta\lambda_{00q}^2$. As $q_{\max}$ increases, more poles appear, but do not greatly change their locations. The higher-q poles that are added correspond only to more short-lived transients whose behavior is not much altered by the decrease in a_0. Only the pole at $s=0$ contributes significantly after a time of order $\eta\lambda_{001}^2$, and gives

$$j_0(t)=E_0/\eta \tag{A6}$$

plus exponentially damped terms. The solution for $j_0(t)$ is seen not be significantly affected by adding larger q values in the axisymmetric modes, and while the shorter-lived transients would eventually become a computational problem at fixed time step if we let $q_{\max}\to\infty$, it is clear that no problems will result in the analytical solution to the system (A2) and (A3).

Finally we compare, in Fig. 13, the results of running the code on the system (A2) and (A3) with the *exact* analytical solution of Eq. (A1) previously described. The deviations of the numerically calculated $j_0(t)$ at different $q_{\max}$ from the analytical solution are plotted. It will be seen that the numerical solutions converge to the analytical solution very well. The influence of different $q_{\max}$ on the solution is limited in a very short period ($t<1$).

[1] J. P. Dahlburg, D. Montgomery, G. D. Doolen, and L. Turner, Phys. Rev. Lett. **57**, 428 (1986); J. Plasma Phys. **37**, 299 (1987); **40**, 39 (1988).

[2] M. L. Theobald, D. Montgomery, G. D. Doolen, and J. P. Dahlburg, Phys. Fluids B **1**, 766 (1989).

[3] D. Montgomery and L. Phillips, Phys. Rev. A **38**, 2953 (1988); Physica D **37**, 215 (1989), in *Maximum Entropy and Bayesian Methods,* edited by P. F. Fougère (Kluwer, Dordrecht, 1990), pp. 281–296.

[4] D. Montgomery, L. Phillips, and M. L. Theobald, Phys. Rev. A **40**, 1515 (1989).

[5] R. G. Storer, Plasma Phys. **25**, 1279 (1983).

[6] S. Chandrasekhar and P. C. Kendall, Astrophys. J. **126**, 157 (1957).

[7] X. Shan, H. Chen, and D. Montgomery, in *Proceedings of a Topical Conference on Research Trends in Nonlinear and Relativistic Effects in Plasmas, La Jolla Institute, 1990,* edited by V. Stefan (AIP, New York, in press).

[8] E. Lorenz, J. Atmos. Sci. **20**, 130 (1963); J. H. Curry, J. R. Herring, J. Longcaric, and S. A. Orszag, J. Fluid Mech. **147**, 1 (1984).

[9] H. Chen, X. Shan, and D. Montgomery, Phys. Rev. A **42**, 6158 (1990).

[10] Z. Yoshida and Y. Giga, Math. Z. **204**, 235 (1990), and Z. Yoshida (unpublished).

[11] J. Wesson, *Tokamaks* (Clarendon, Oxford, 1987).

[12] H. A. B. Bodin and A. A. Newton, Nucl. Fusion **20**, 1255 (1980).

[13] C. Canuto, M. Y. Hussaini, A. Quarteroni, and T. A. Zang, *Spectral Methods in Fluid Dynamics* (Springer-Verlag, New York, 1987), Chap. 1.

[14] C. W. Gear, *Numerical Initial-Value Problems in Ordinary Differential Equations* (Prentice-Hall, Englewood Cliffs, NJ, 1971), Chaps. 7 and 11.

[15] S. Cappello and R. Paccagnella, in *Turbulent Plasma Sustainment in the Reverse Field Pinch,* Proceedings of the Varenna Summer School "Piero Caldirola," Varenna, 1990, edited by E. Sindoni, F. Troyon, and J. Vaclavik (Societa Italiana di Fisica, Bologna, 1990).

[16] D. A. Baker, C. J. Buchenauer, L. C. Burkhardt, T. E. Cayton, E. J. Caramana, G. I. Chandler, R. S. Christian, R. Dagazian, J. N. DiMarco, J. N. Downing, J. P. Freidberg, R. F. Gribble, R. A. Gerwin, D. W. Hewett, R. B. Howell, A. R. Jacobson, F. C. Jahoda, J. Killeen, K. A. Klare, H. R. Lewis, E. M. Little, L. W. Mann, G. Miller, R. W. Moses, R. A. Nebel, S. Ortolani, R. B. Paris, J. A. Phillips, D. D. Schnack, A. E. Schofield, K. S. Thomas, R. G. Watt, P. G. Weber, J. A. Wesson, R. Wilkins, and Y. Yoshida, in *Proceedings of the 8th International Conference on Plasma Physics and Controlled Fusion Research, Brussels, 1980* (IAEA, Vienna, 1981), Vol. II, p. 291.

[17] J. A. Snipes, D. J. Campbell, P. S. Haynes, T. C. Hender, M. Hugon, P. J. Lomas, N. J. Lopes Cardozo, M. F. F. Nave, and F. C. Schüller, Nucl. Fusion **28**, 1085 (1988).

[18] A. Weller, A. D. Cheetham, A. W. Edwards, R. D. Gill, A. Gondhalekar, R. S. Granetz, J. Snipes, and J. A. Wesson, Phys. Rev. Lett. **39**, 2303 (1987).

[19] D. Montgomery, in *Trends in Theoretical Physics,* edited by P. J. Ellis and Y. C. Tang (Addison-Wesley, New York, 1990), Vol. I, pp. 239–262.

[20] J. B. Taylor, Phys. Rev. Lett. **33**, 1139 (1974); Rev. Mod. Phys. **58**, 741 (1986).